# Study of IPMSM Interturn Faults Part II: Online Fault Parameter Estimation

Bon-Gwan Gu

***Abstract*—This paper is a continuation of part I, which presented interturn fault (ITF) models for interior permanent magnet synchronous motors (IPMSMs). ITFs are defined by two ITF parameters: the healthy turn ratio and the fault contact resistance. First, this paper presents a proof that the two fault parameters defining a given ITF condition cannot be individually estimated from motor information and drive information (applied voltage, phase current, rotor speed, etc.) because they have multiple solutions. However, it is also shown that the additional Ohmic loss, which is the most important factor in heat generation and deterioration due to ITFs, is not dependent on these solutions. Thus, after arbitrarily setting one fault parameter, the other can be estimated for a given ITF condition; this model can be used to represent the effect of an ITF, particularly its Ohmic power loss. In this paper, an online fault parameter estimation method for IPMSMs is proposed after presenting one of the two fault parameters. The proposed method utilizes a searching algorithm that finds the fault parameter that has the minimum negative-sequence voltage error between the applied voltage and the ITF models (presented in part I). An experiment was performed to verify the proposed fault parameter estimation method.**

***Index Terms*—Fault parameter estimation, inter-turn fault (ITF), motor fault detection, motor fault-tolerant control.**

## I. Introduction

MOTOR fault detection is a primary issue because faults can lead to reduced safety and increased repair time costs [1], [2]. As stated in part I, the most common motor fault is a winding interturn fault (ITF) due to coil insulation failure. The detection of stator ITFs in different types of electric machines, such as on induction motors [3]–[13], brushless DC motors [14]–[16], claw-pole generators [17], and synchronous motors [18]–[23] has been performed in many studies.

Detection methods can be categorized into three types, based on the selected fault signatures.

1) Unbalanced signals resulting from unbalanced impedance and backelectromotive force (EMF): An ITF causes an unbalanced motor impedance and back-EMF that eventually induce unbalanced motor currents and voltages. In many previous studies, the unbalanced impedance, back-EMF, current, and voltage of motors have been the most commonly used fault detection signals.

Manuscript received May 24, 2015; revised August 9, 2015 and September 30, 2015; accepted November 23, 2015. Date of publication December 17, 2015; date of current version May 20, 2016. This work was supported by the National Research Foundation of Korea (NRF) Grant funded by the Korea government (MSIP) (2015R1C1A1A01052647). Recommended for publication by Associate Editor F. H. Khan.

The author is with the School of Energy Engineering, Kyungpook National University, Daegu 702-701, Korea (e-mail: bggu@knu.ac.kr).

Color versions of one or more of the figures in this paper are available online at http://ieeexplore.ieee.org.

Digital Object Identifier 10.1109/TPEL.2015.2506640

a) Unbalanced current [4]–[6] [10], [13], [17], [19], [21].
The unbalanced current is a useful signal for ITF detection because it is easy to calculate from the phase current. In a conventional ITF detection scheme, the unbalanced current is calculated after the phase current has been sensed. Then, the ITF decision rule is used to compare the unbalanced current with the predefined fault limit value from a lookup table; lookup tables are created for various drive conditions using a rich pretest dataset.
By monitoring the Park's vector of the motor current, the unbalanced current due to an ITF can be observed. Cardoso *et al.* [4] proposed an online diagnosis method that uses an ellipticity check for operating three-phase induction machines. The unbalanced current can also be observed in the $abc$ frame in the ellipse form, which is similar to Park's vector [13]. Hadef *et al.* [21] used the direct torque control approach to apply a pattern recognition technique based on image composition to interior permanent magnet synchronous motors (IPMSMs). The unbalanced current can be observed in the form of a negative-sequence current or second harmonic current in the positive synchronous reference frame (SRF). Arkan *et al.* [5] and Kim *et al.* [19] used the negative-sequence current and the second harmonic current as the main signals for fault diagnosis. Briz *et al.* [6] utilized the negative-sequence current resulting from high-frequency carrier-signal injection to detect ITFs. The unbalanced current can be observed in the third current harmonic at the dc-link side. This method has also been utilized for fault detection in claw-pole generators [17].

b) Negative-sequence/transfer impedance or unbalanced back-EMF [7], [8], [11], [12], [16], [23].
The fault detection methods proposed in [7], [8], and [11] can be explained in terms of the negative-sequence impedance and transfer impedance by including the effects of nonidealities. The estimated impedance is utilized as a fault detection signal. Tallam *et al.* [7] proposed a neural-network (NN)-based detection scheme to reduce the amounts of data memory usage and computation. Ostojic *et al.* [12] utilized the normalized cross-coupled impedance (ratio of cross-coupled impedance and positive-sequence impedance) as the key signal for fault detection. Park *et al.* [16] used the phase impedance of

brushless DC motors as the key signal for ITF detection. Sarikhani and Mohammed [23] compared the normalized back-EMF difference between values estimated in real time and reference values from finite element analysis for fault detection.

c) Line-neutral voltages [3], [10], [14].
Cash *et al.* [3] and Awadallah *et al.* [14] used the sum of the three instantaneous line-neutral voltages to detect an ITF. Yun *et al.* [10] proposed an online monitoring technique for detecting and classifying ITFs and high-resistance connections in an induction motor, based on the neutral point voltage and negative-sequence current measurements.

2) High-order harmonic current [18], [20]: Neti and Nandi [18] and Ebrahimi and Faiz [20] introduced frequency patterns for a synchronous motor with field windings and a permanent magnet synchronous motor (PMSM) with ITFs. Frequency pattern analysis is commonly used for the grid-connected induction motor ITF detection. However, for inverter-driven motors, the high frequency of the inverter PWM voltage interferes with the fault detection frequency. Therefore, frequency pattern analysis is not commonly used for inverter-driven motors.
3) Induced voltage in additional coil [15]: Kim *et al.* [15] proposed a detection coil for sensing the flux variation caused by the ITF. This method is simple, but it requires an additional detection coil installed within the motor.

The detection tools of previous works can generally be classified into lookup table schemes and NN-based schemes [9], [22]. Because the lookup-table-based detection schemes are easy to implement, they have been utilized in many studies. However, they require a fault threshold level table to be built based on rich pretest data because of the absence of accurate IPMSM models that include ITFs. To overcome this disadvantage, NN-based schemes have been proposed. NN-based schemes do not need any tables, but they do require a training phase. If an accurate ITF model of an IPMSM is derived, the pretest to define the threshold level or training phase for the NN will be much simpler. Hence, to implement an ITF detection method for a specific motor, an adequate IPMSM model including ITFs must be derived.

This paper proposes an online ITF parameter estimation method for IPMSMs using the ITF models proposed in part I. Because the ITF fault decision rule should be based on the threshold limit set for the fault parameter based on the motor heat radiation structure and operation environment, we focus on the fault parameter estimation method. First, it is proven that the two ITF parameters, namely, the healthy turn ratio and the fault contact resistance, cannot be separately estimated based on drive information because they have multiple solutions. Nevertheless, these multiple solutions theoretically have the same ITF Ohmic power loss, which is the key index used to define the additional internal heat generation and fault severity for the motor. Both parameters do not need to be estimated to obtain the Ohmic power loss. Thus, the proposed method estimates only one fault parameter by allowing the other to be set arbitrarily. Here, we set the fault resistance to zero in the simpler model, and the healthy turn ratio will be an estimation parameter. The estimation method implements a searching algorithm that finds one fault parameter that satisfies the minimum negative-sequence voltage difference between the drive voltage information and the ITF model. An experiment was performed to verify the proposed fault parameter estimation method.

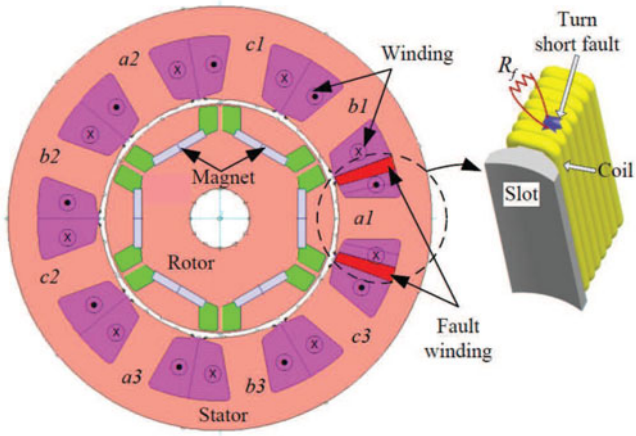


Fig. 1. Cross-sectional image of six-pole nine-slot IPMSM with an ITF.

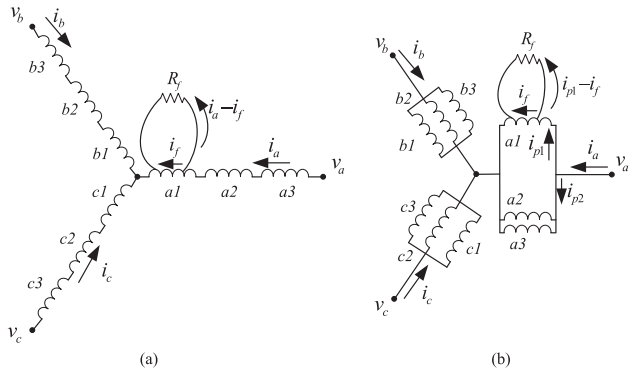


Fig. 2. (a) Series-connected and (b) parallel-connected winding configurations with ITF.

## II. ITF Analysis of One Winding

Fig. 1 shows a cross-sectional view of a six-pole nine-slot IPMSM with concentric windings. Here, $a1$, $a2$, $a3$, $b1$, $b2$, $b3$, $c1$, $c2$, and $c3$ are the winding numbers of each phase. Fig. 2 shows the winding configuration of (a) series and (b) parallel connections. $i_a$, $i_b$, and $i_c$ denote the phase currents; and $v_a$, $v_b$, and $v_c$ denote the voltages of the $a$-, $b$-, and $c$-phase windings, respectively. Because an insulation failure does not provide a zero resistance path [1], [2], the fault location can be described as a fault resistance $R_f$ with an ITF current $i_f$. In this study, the $a$-phase $a1$ winding is assumed to have an ITF. The ITF windings shown in Fig. 2 have another fault circuit loop composed of the fault resistance $R_f$, a fault winding inductance, and a fault winding flux linkage.

When the IPMSM has an ITF, negative-sequence elements exist in the voltage and current. However, because the models

proposed in part I are derived under the assumption of a balanced three-phase current, all of the unbalanced phase impedances and phase back-EMFs affect only the motor voltage, which is modeled by the negative-sequence voltage equations in the negative SRF. The assumed balanced three-phase currents are expressed as

$$i_a = -I_q \sin\theta + I_d \cos\theta \tag{1}$$

$$i_b = -I_q \sin\left(\theta - \frac{2\pi}{3}\right) + I_d \cos\left(\theta - \frac{2\pi}{3}\right) \tag{2}$$

$$i_c = -I_q \sin\left(\theta + \frac{2\pi}{3}\right) + I_d \cos\left(\theta + \frac{2\pi}{3}\right) \tag{3}$$

where $\theta$ denotes the electrical rotor angle, and $I_d$ and $I_q$ are the $dq$-axis currents in the SRF. The negative-sequence voltage equations of IPMSMs employing series and parallel winding connections were derived in part I and are presented here: (4), (5) shown at bottom of the page. $R_{\rm sij}$, $k_{\rm sij}$, $R_{\rm pij}$, and $k_{\rm pij}$ are defined with motor and fault parameters in part I. Here, $i, j = 1, 2, 3, 4$. The healthy turn ratio is $x$. The fault resistance is $R_f$. $\omega(= d\theta/dt)$ and $\psi_m$ denote the electrical angular velocity and back-EMF constant, respectively. $\alpha_{s1,2}$, $\beta_{p1,2}$, and $\alpha_{p1,2}$ represent the sine and cosine magnitudes of the fault current $i_f$ for both the series and parallel winding IPMSMs and the $a1$ winding current $i_{p1}$ of the parallel winding IPMSM. $i_f$ and $i_{p1}$ can be expressed as follows:

$$i_f = \alpha_{s1}\sin\theta + \alpha_{s2}\cos\theta : \text{series winding IPMSM} \tag{6}$$

$$\left.\begin{aligned} i_{p1} &= \alpha_{p1}\sin\theta + \alpha_{p2}\cos\theta \\ i_f &= \beta_{p1}\sin\theta + \beta_{p2}\cos\theta \end{aligned}\right\} : \text{parallel winding IPMSM.} \tag{7}$$

The healthy turn ratio of $a1$ is defined as $x = N_{\rm healthy}/N$, where $N_{\rm healthy}$ and $N$ denote the $a1$ winding's healthy turn number and total turn number, respectively.

The ITF is resolved into two fault parameters: the healthy turn ratio $x$ and the fault resistance $R_f$. Because these two parameters define the fault severity, they should be estimated for better fault detection accuracy and the creation of a more fault-tolerant drive.

Fig. 3 shows the negative-sequence voltage plots of (a) series and (b) parallel winding IPMSMs with (4) and (5) when the ITF exists in the $a$-, $b$-, or $c$-phase windings. The negative-sequence voltages for $a$-, $b$-, and $c$-phase winding faults have phase differences of $2\pi/3$ relative to each other. Table I presents the motor parameters, which are the same as those of the motors described in part I. $L_1$, $L_2$, and $\gamma$ were obtained from FEM simulations [2]. As shown in Fig. 3, for a given motor speed and phase current, the absolute value of the negative-sequence voltage increases along a curve as $x$ increases or $R_f$ decreases. In other words, for a given point on the negative-sequence voltage plot, there are multiple solutions $x$ and $R_f$ that satisfy both (4) and (5). Thus, the two fault parameters $x$ and $R_f$ cannot be individually calculated or estimated using the model proposed in part I; however, an equation relating them can be obtained. In this section, we develop unbalanced voltage equations for a single winding with an ITF to show that the two fault parameters $x$ and $R_f$ cannot be individually estimated based on the unbalanced voltage. Then, we present the equation relating $x$ and $R_f$ and derive the additional Ohmic power loss.

### A. Unbalanced Voltage of One Winding

Fig. 4 shows an $a1$ winding with an ITF and its equivalent circuit, where $\mathbf{v_{a1}}$, $\mathbf{i_{a1}}$, and $\mathbf{\Lambda_{a1}}$ denote the $a1$-winding voltage, $a1$-winding current, and total cross-flux linkage of both the other windings and the rotor flux in the complex domain, respectively. $R_{a1}$ and $L_{a1}$ denote the $a1$ winding resistance and inductance, respectively. The faulty windings and the remaining healthy windings have turn numbers of $N(1-x)$ and $Nx$, respectively. Because of the ITF's resistance $R_f$, the faulty and healthy windings have different current magnitudes and phases. Because the two windings are placed in the same

$$\begin{bmatrix} V_{\rm de}^- \\ V_{\rm qe}^- \end{bmatrix} = \frac{1}{3}\begin{bmatrix} \begin{pmatrix} (R_{s11}-R_{s22})I_d + R_{s14}\alpha_{s2} + \omega L_1(k_{s14}-k_{s24})\alpha_{s1} \\ +\omega L_1(-k_{s11}+2k_{s12}+k_{s22}-2k_{s23})I_q \end{pmatrix} \\ \begin{pmatrix} -(R_{s11}+2R_{s22})I_q + R_{s14}\alpha_{s1} - \omega L_1(k_{s14}-k_{s24})\alpha_{s2} \\ +\omega L_1(-k_{s11}+2k_{s12}+k_{s22}-2k_{s23})I_d + \frac{2}{P}(1-x)\omega\psi_m \end{pmatrix} \end{bmatrix} + \frac{\omega L_2}{6}\begin{bmatrix} (-k_{s11}+2k_{s12}+k_{s22}-2k_{s23})I_q + (k_{s14}+2ks24)\alpha_{s1} \\ (k_{s11}-2k_{s21}-k_{s22}+2k_{s23})I_d + (k_{s14}+4ks24)\alpha_{s2} \end{bmatrix} \tag{4}$$

$$\begin{bmatrix} V_{\rm de}^- \\ V_{\rm qe}^- \end{bmatrix} = \frac{1}{3}\begin{bmatrix} \begin{pmatrix} (R_{p22}-R_{p33})I_d + \omega L_1(-k_{p22}+2k_{p23}-2k_{p34}+k_{p33})I_q \\ +\omega L_1(k_{p21}-k_{p22}-k_{p31}+k_{p32})\alpha_{p1} - R_{p22}\alpha_{p2} + \omega L_1(k_{p25}-k_{p35})\beta_{p1} \end{pmatrix} \\ \begin{pmatrix} (-R_{p22}+R_{p33})I_q + \omega L_1(-k_{p22}+2k_{p23}+k_{p33}-\frac{k_{p34}}{2})I_d \\ +\omega L_1(-k_{p21}+k_{p22}+k_{p31}-k_{p32})\alpha_{p2} - R_{p22}\alpha_{p1} + \omega L_1(-k_{p25}+k_{p35})\beta_{p2} \end{pmatrix} \end{bmatrix} + \frac{\omega L_2}{6}\begin{bmatrix} (k_{p21}-k_{p22}+2k_{p31}-2k_{p32})\alpha_{p1} - (k_{p22}+2k_{p32})I_q + (2k_{p35}+k_{p25})\beta_{p1} \\ (k_{p21}-k_{p22}+2k_{p31}-2k_{p32})\alpha_{p2} + (k_{p22}+2k_{p32})I_d + (2k_{p35}+k_{p25})\beta_{p2} \end{bmatrix} \tag{5}$$

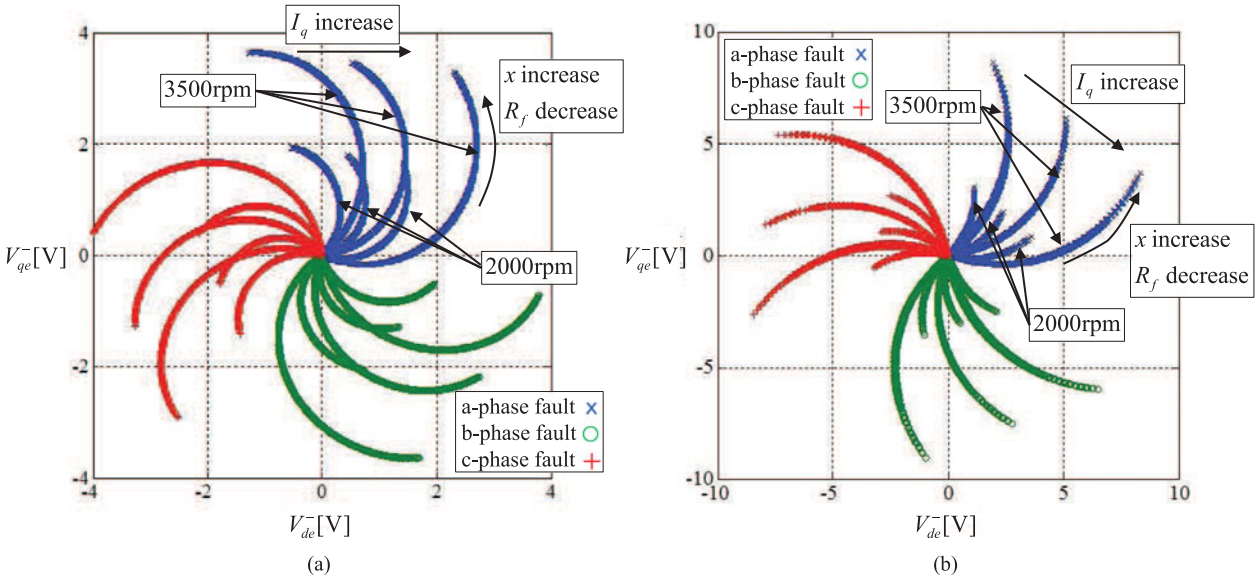


Fig. 3. Negative-sequence voltage plots for $a$-, $b$-, and $c$-phase faults for $I_q = -10$, 0, and 10 A and $0.5 < x < 1$: (a) series winding IPMSM for $0.001 < R_f < 0.1\,\Omega$ and (b) parallel winding IPMSM for $0.1 < R_f < 1\,\Omega$.

TABLE I
MOTOR SPECIFICATIONS

| Items | Values | Units |
|---|---|---|
| Pole number | 6 | |
| Rated phase current | 10 | [$A_{\text{peak}}$] |
| Rated phase-to-phase voltage | 27 | [$V_{\text{rms}}$] |
| $L_1$ | 702 | [$\mu$H] |
| $L_2$ | 147 | [$\mu$H] |
| Phase resistance $R$ | 0.129 | [$\Omega$] |
| Healthy turn ration $x$ | 0.5833 | |
| Coupling factor | 0.15135 | |

magnetic flux path, they are coupled to each other as described by $j\omega x(1-x)L_{a1}\mathbf{i_{a1}}$ and $j\omega x(1-x)L_{a1}\mathbf{i_f}$ in Fig. 4. When $x$ and $R_f$ are not equal to 1 and an infinite value, respectively, a faulty circuit and an unbalanced voltage exist. The unbalanced voltage generates a negative-sequence voltage, as described in (4) and (5), and decreases the positive-sequence voltage, as described in part I.

From Fig. 4, the voltage equations for two closed loops can be derived as follows:

$$\mathbf{v_{a1}}(x) = (R_{a1} + j\omega L_{a1})(x\mathbf{i_{a1}} + (1-x)\mathbf{i_f}) + j\omega\mathbf{\Lambda_{a1}} \quad (8)$$

$$0 = \left[(1-x)R_{a1} + j\omega(1-x)^2 L_{a1}\right]\mathbf{i_f} + j\omega x(1-x) \times L_{a1}\mathbf{i_{a1}} + j\omega(1-x)\mathbf{\Lambda_{a1}} - R_f(\mathbf{i_{a1}} - \mathbf{i_f}). \quad (9)$$

When the PMSM has no ITF ($x = 1$), the $a1$-winding voltage $\mathbf{v_{a1}}(x=1)$ has no element that induces unbalanced voltage in the model. Thus, by subtracting $\mathbf{v_{a1}}(x)$ from $\mathbf{v_{a1}}(x=1)$, the unbalanced voltage term can be derived from (8) and (9)

$$\mathbf{v_{a1}}(x=1) - \mathbf{v_{a1}}(x) = (R_{a1} + j\omega L_{a1})\left[(R_{a1} + j\omega L_{a1})\mathbf{i_{a1}} + j\omega\mathbf{\Lambda_{a1}}\right]\frac{1}{j\omega L_{a1} + f_{\text{xR}}(x, R_f)} \quad (10)$$

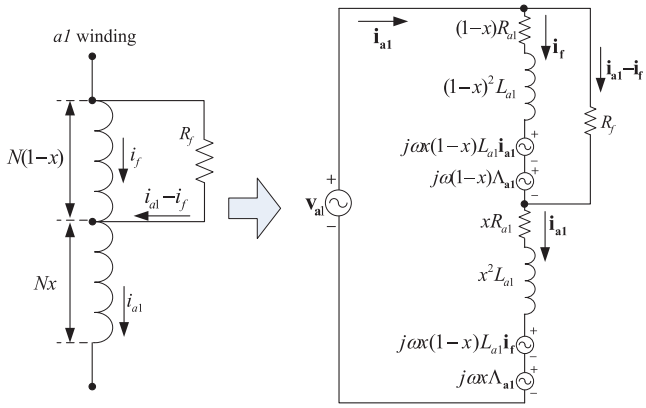


Fig. 4. $a1$ winding with ITF and equivalent circuit.

where $f_{\text{xR}}(x, R_f)$ can be defined as follows:

$$f_{\text{xR}}(x, R_f) = \frac{R_{a1}}{(1-x)} + \frac{R_f}{(1-x)^2}. \quad (11)$$

In the same manner, the unbalanced flux due to the faulty $a1$ winding, which affects other windings, can be calculated as follows:

$$\mathbf{\Phi_{o-a1}}(x=1) - \mathbf{\Phi_{o-a1}}(x) = \frac{L_{a1}\mathbf{i_{a1}} - (1-x)L_{a1}\mathbf{i_f} - xL_{a1}\mathbf{i_{a1}}}{N}$$

$$= \frac{L_{a1}}{N}\left[(R_{a1} + j\omega L_{a1})\mathbf{i_{a1}} + j\omega\mathbf{\Lambda_{a1}}\right]\frac{1}{j\omega L_{a1} + f_{\text{xR}}(x, R_f)} \quad (12)$$

where $\mathbf{\Phi_{o-a1}}$ denotes the total flux generated by the $a1$ winding. Because the coupling coefficient is dependent on the winding placement, the coupled flux linkage from the $a1$ winding to the other windings is proportional to $\mathbf{\Phi_{o-a1}}$. Therefore, the coupled unbalanced voltage from the faulty $a1$ winding to other windings is proportional to (12).

The total unbalanced voltage is generated by summing the unbalanced voltages between the faulty $a1$ winding (10) and

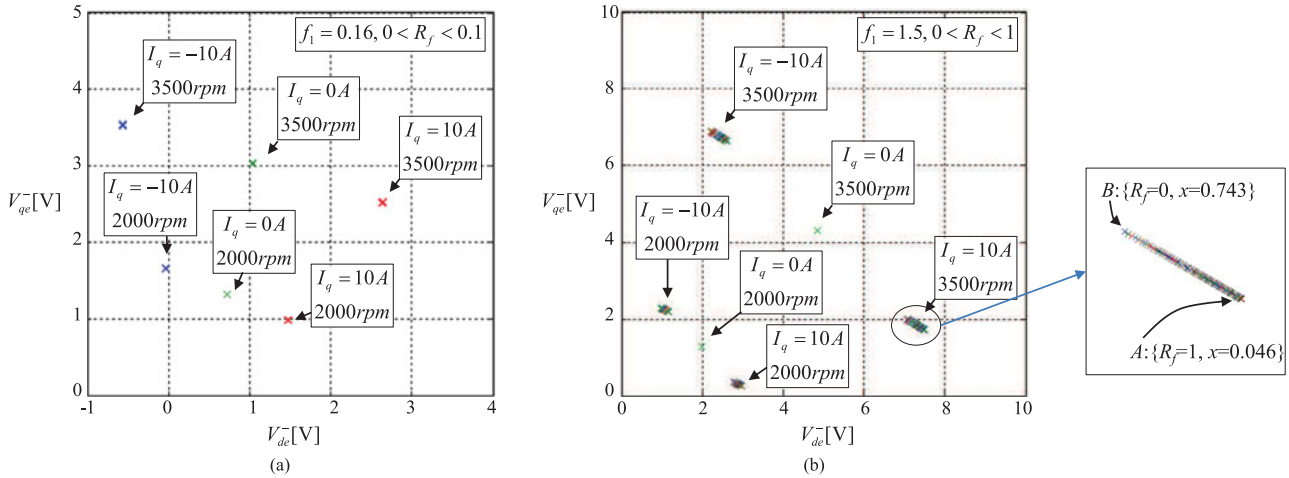


Fig. 5. Plots of calculated negative-sequence voltage for (a) series winding with $f_{\mathrm{xR}} = 0.161$, $0 < R_f < 0.1$ and (b) parallel winding with $f_{\mathrm{xR}} = 1.505$, $0 < R_f < 1$, and $x$ calculated with (13).

the other (healthy) windings, induced by the unbalanced coupled flux linkage according to (12). Note that both (10) and (12) are proportional to $1/(j\omega L_{a1} + f_{\mathrm{xR}}(x, R_f))$. As a result, the total unbalanced voltage is proportional to $1/(j\omega L_{a1} + f_{\mathrm{xR}}(x, R_f))$ and, thus, is a function of $f_{\mathrm{xR}}(x, R_f)$. Except for via $f_{\mathrm{xR}}(x, R_f)$, the total unbalanced voltage is independent of fault parameters $x$ and $R_f$. For a given ITF condition, $x$ and $R_f$ are constant values. Thus, $f_{\mathrm{xR}}$ is also a constant value by (11); its value is maintained unless fault parameter variation occurs. Thus, from the total unbalanced voltage, constant $f_{\mathrm{xR}}$ can be identified; however, there are multiple $x$ and $R_f$ solutions for a given constant value of $f_{\mathrm{xR}}(x, R_f)$.

Fig. 5 shows the calculated negative-sequence voltage based on the ITF model: (a) series winding with $f_{\mathrm{xR}} = 0.161$ and different values of $0 < R_f < 0.1$ and (b) parallel winding with $f_{\mathrm{xR}} = 1.505$ and different values of $0 < R_f < 1$. The healthy winding ratio $x$ is calculated from (11)

$$x = 1 - \frac{R_{a1} + \sqrt{R_{a1}^2 + 4R_f}}{2f_{\mathrm{xR}}} \tag{13}$$

where $R_{a1}$ is the resistance of one winding. Here, because the number of phase windings in each of the studied motors is $P/2$, $R_{a1} = \frac{2R}{P}$ and $R_{a1} = \frac{PR}{2}$ for series and parallel winding IPMSMs is satisfied, respectively, where $P$ and $R$ denotes the pole number and phase resistance. As shown in Fig. 5, the negative-sequence voltages are placed near each other for a fixed current and speed at various $R_f$ and $x$ values that satisfy (13). Thus, the negative-sequence voltage $[V_{\mathrm{de}}^-\ V_{\mathrm{qe}}^-]$ is the same if $f_{\mathrm{xR}}$ is constant. This means that $x$ and $R_f$ cannot be obtained or estimated from a given unbalanced or negative-sequence voltage.

However, note that $i_{a1}$ is equal to $i_a$ and $i_{p1}$ for the series and parallel winding IPMSM. Therefore, the total unbalanced voltage is a function of $i_a$ and $i_{p1}$. $i_a$ is a known value (and is controllable), but $i_{p1}$ is not known. If $i_{p1}$ varies under a constant value of $f_{\mathrm{xR}}$ and different values of the fault parameters, and its variation could meaningfully affect the negative sequence, $x$ and $R_f$ can be estimated individually from the negative-sequence voltage.

To observe $i_{p1}$ and $[V_{\mathrm{de}}^-\ V_{\mathrm{qe}}^-]$ variation ranges for a range of $x$ and $R_f$ values, we determined the two fault conditions having the maximum difference under $I_q = 10$ A and 3500 r/min in Fig. 5(b), which exist at $A : \{R_f = 1,\ x = 0.046\}$ and $B : \{R_f = 0, x = 0.743\}$. These values are the maximum and minimum for the given range of $0 \le R_f \le 1$; the negative-sequence voltages for these values are located at the edge of the point group, as shown on the right-hand side of Fig. 5(b). The calculated $(\alpha_{p1}, \alpha_{p2})$ values of $i_{p1}$ are $(1.51, -16.06)|_A$. and $(2.05, -15.39)|_B$.. If $I_q = 0$, no difference in $i_{p1}$ for various $x$ and $R_f$ values is observed; therefore, $[V_{\mathrm{de}}^-\ V_{\mathrm{qe}}^-]$ have the same value, as in the results of the series winding IPMSM shown in Fig. 5(a). However, because of the difference of $i_{p1}$ for nonzero values of $I_q$, one can observe that the negative-sequence voltage has differences with different $x$ and $R_f$ values, as shown in Fig. 5(b). Nevertheless, the maximum differences in $i_{p1}$ and $[V_{\mathrm{de}}^-\ V_{\mathrm{qe}}^-]$ between these two $A$ and $B$ conditions are less than 7%. For simplicity, we assume that $i_{p1}$ is not influenced by individual $x$ and $R_f$ values. Hence, $[V_{\mathrm{de}}^-\ V_{\mathrm{qe}}^-]$ is also assumed to be a function of $f_{\mathrm{xR}}$ in the case of the parallel winding IPMSM.

Because the fault parameters should be limited to $0 \le x \le 1$ and $R_f \ge 0$, $f_{\mathrm{xR}}$ is a positive value. The equation relating $x$ and $R_f$ can be rewritten as follows:

$$\begin{aligned} R_f &= f_{\mathrm{xR}}(1-x)^2 - (1-x)R_{a1} \\ &= (1-x)(f_{\mathrm{xR}} - R_{a1} - f_{\mathrm{xR}}x). \end{aligned} \tag{14}$$

Fig. 6 shows the $\hat{R}_f$ and $\hat{x}$ estimation process based on the negative-sequence voltage. On the right-hand side of Fig. 6, a graph of the parabola quadrature function (14) is shown. From the observed negative-sequence voltage, possible $R_f$ and $x$ values are placed along the solid line in the $R_f \ge 0$ and $0 \le x \le 1$ range.

### B. Additional Ohmic Power Loss due to ITF

Because the ITF current induces additional Ohmic power loss and heat in the faulty winding, it must be quantified. In the series winding IPMSM, the additional power loss $P_f$ occurs at $R_f$ and

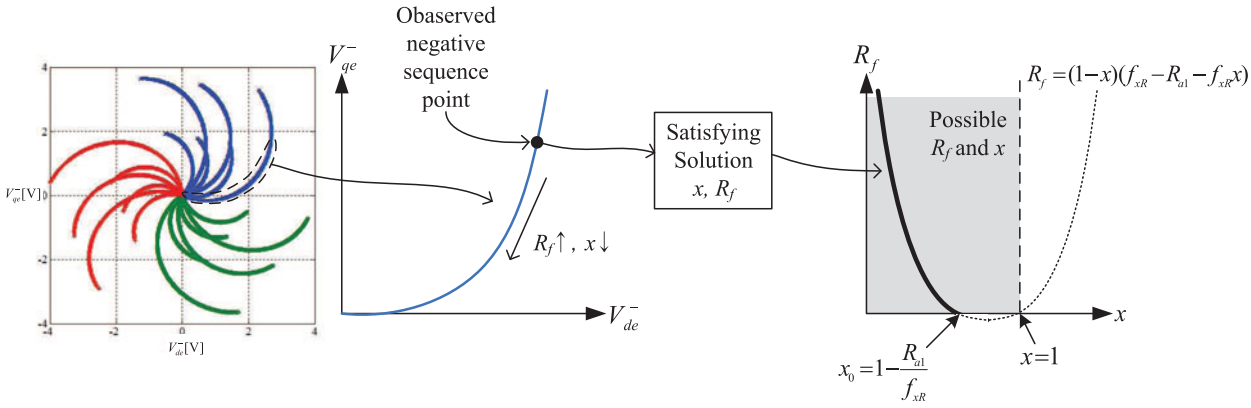


Fig. 6. Multiple solutions for a given negative-sequence voltage.

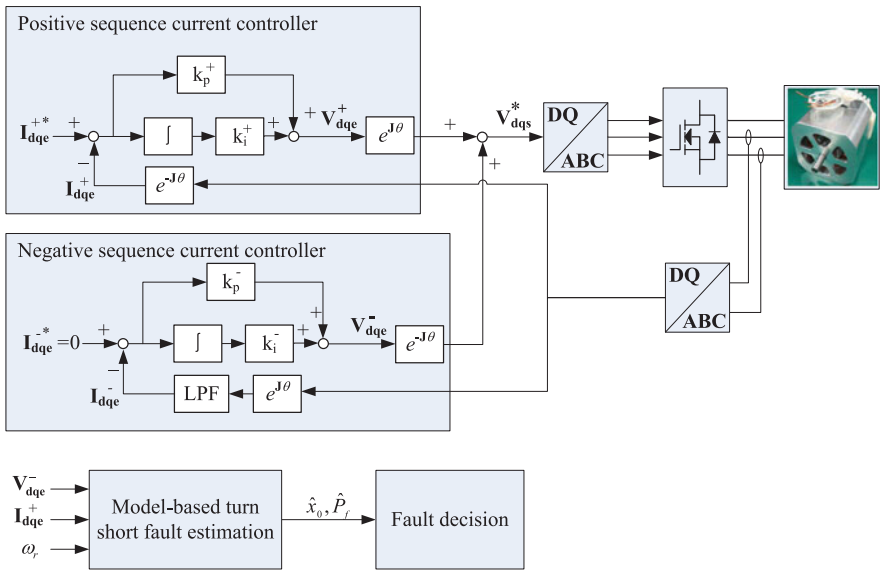


Fig. 7. Control block diagram with negative-sequence current controller.

$R_{a1}$; it is derived as follows:

$$P_f = \frac{1}{2}(\mathbf{i_a}-\mathbf{i_f})(\mathbf{i_a}-\mathbf{i_f})^* R_f + \frac{1}{2}(\mathbf{i_f}\mathbf{i_f}^* - \mathbf{i_a}\mathbf{i_a^*})R_{a1}(1-x)$$
$$= \frac{f_{\mathrm{xR}}}{2}\frac{[\mathbf{\Lambda_{a1}} + (R_{a1}+j\omega L_{a1})\mathbf{i_a}]\,[\mathbf{\Lambda_{a1}^*} + (R_{a1}-j\omega L_{a1})\mathbf{i_a}^*]}{f_{\mathrm{xR}}^2+\omega^2 L_{a1}^2} + \frac{\mathrm{Re}\,\{(\mathbf{\Lambda_{a1}} + R_{a1}\mathbf{i_a})(j\omega L_{a1} - f_{\mathrm{xR}})\mathbf{i_a}^*\}\,R_{a1} - \omega^2 L_{a1}^2 R_{a1}\mathbf{i_a}\mathbf{i_a^*}}{f_{\mathrm{xR}}^2+\omega^2 L_{a1}^2}. \quad (15)$$

Equation (15) shows that the $P_f$ value of the series winding IPMSM is a function of $f_{\mathrm{xR}}$.

For the parallel winding IPMSM, $i_{p1}(=i_{a1})$ changes, depending on the drive and ITF condition. Therefore, the additional power loss is obtained by subtraction of the normal Ohmic loss $\frac{1}{2}\mathbf{i_a}\mathbf{i_a^*}R$ from the overall Ohmic loss

$$P_f = \frac{1}{2}(\mathbf{i_{p1}}-\mathbf{i_f})(\mathbf{i_{p1}}-\mathbf{i_f})^* R_f + \frac{1}{2}(\mathbf{i_f}\mathbf{i_f}^* - \mathbf{i_{p1}}\mathbf{i_{p1}^*})R_{a1}(1-x) + \frac{1}{2}\mathbf{i_{p1}}\mathbf{i_{p1}^*}R_{a1} + \frac{1}{2}\mathbf{i_{p2}}\mathbf{i_{p2}}^*\frac{PR}{P-2} - \frac{1}{2}\mathbf{i_a}\mathbf{i_a^*}R. \quad (16)$$

The first and second term on the right-hand side of (16) can be derived as a function of $f_{\mathrm{xR}}$ in the same manner as (15). Because we assumed that $i_{p1}$ does not influence individual $x$ and $R_f$ values, the additional Ohmic power loss $P_f$ in a parallel winding IPMSM is assumed to be a function of $f_{\mathrm{xR}}$.

According to (15) and (16), the fault current power loss $P_f$ is a function of $f_{\mathrm{xR}}$; as a result, the total fault power loss can be calculated without having exact values for $x$ and $R_f$, although the heating region and density vary according to $x$ and $R_f$. $P_f$ represents the additional loss caused by an ITF; thus, it is zero for a healthy motor. This Ohmic power loss increases the total power loss in the system and the motor winding temperature, which is a major reason for the expansion of the fault winding range. Thus, depending on the additional Ohmic power loss $P_f$, a fault level should be established and a fault-tolerant drive could limit the possible drive speed and torque ranges.

## III. ITF Parameter Estimation

This section presents an ITF parameter estimation method that applies a searching algorithm to the ITF model. The primary problem caused by an ITF is additional Ohmic power loss

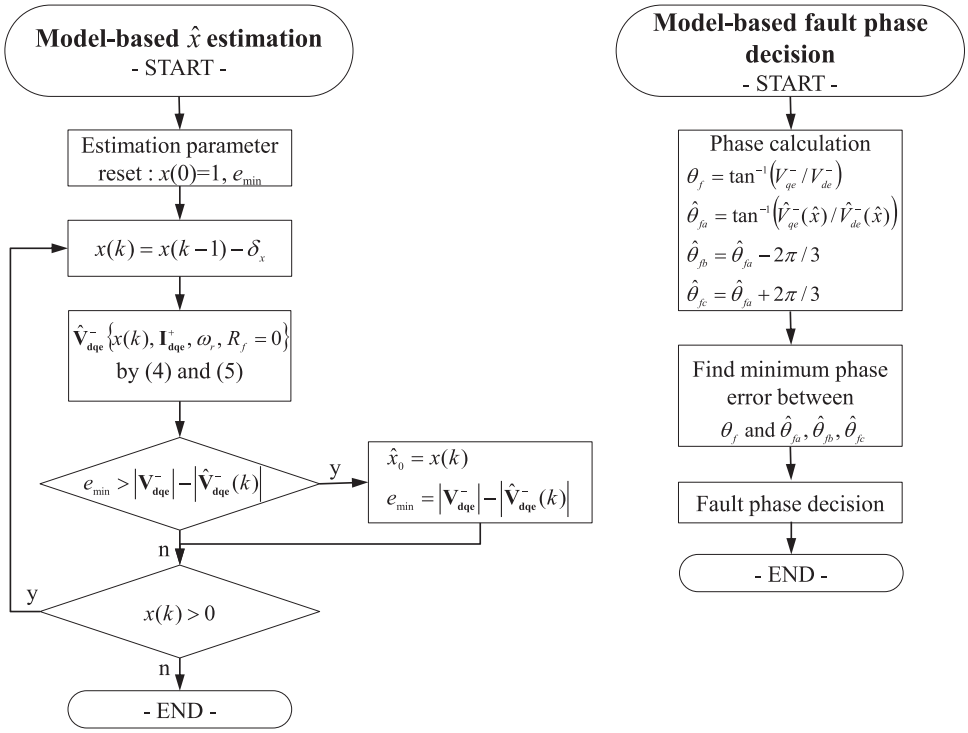


Fig. 8. Flowcharts: (a) proposed $x$ estimation method under the assumption that $R_f = 0$, (b) proposed faulty phase decision method.

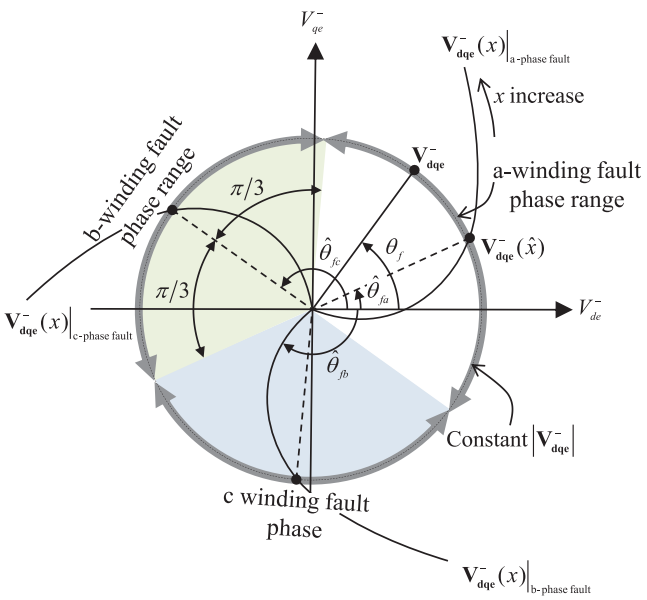


Fig. 9. Plot of negative-sequence voltage phase $\theta_f$ and calculated negative-sequence voltage phases $\theta_{\rm fa}$, $\theta_{\rm fb}$, and $\theta_{fc}$ for $a$-, $b$-, and $c$-phase faults, respectively, based on (4) and (5) in the negative SRF.

and internal heat generation, both of which worsen the fault condition. The previous section presented a proof that the additional power loss is independent of $x$ and $R_f$ if $f_{\rm xR}$ is constant. If we choose arbitrary values of $x$ and $R_f$ that satisfy the condition of having a constant value of $f_{\rm xR}$, the additional power loss would be the same. Thus, by letting $R_f = 0$, the unbalanced voltage equations (4) and (5) are simplified; $x_0 (= x|_{R_f=0})$ is easily obtained with a searching algorithm. $x_0$ is utilized to represent the ITF severity.

Fig. 7 shows the overall control block diagram, where $\mathbf{V}^+_{\rm dqe}$, $\mathbf{V}^-_{\rm dqe}$, $\mathbf{I}^+_{\rm dqe}$, and $\mathbf{I}^-_{\rm dqe}$ denote the positive voltage, negative voltage, positive current, and negative current in the SRF, respectively. $\mathbf{V}^*_{\mathbf{dqs}}$ and $\omega_r$ denote the voltage command in the stationary $dq$ reference frame and the rotor angular velocity, respectively; the superscript $*$ denotes a reference value. The positive- and negative-sequence current controllers are applied to create the balanced three-phase current [1], [2]. At the bottom of Fig. 7, the proposed fault parameter estimation method and fault decision block diagram are shown. The proposed fault parameter estimator utilizes the negative-sequence voltage $\mathbf{V}^-_{\rm dqe} = [V^-_{\rm de}\ V^-_{\rm qe}]^T$, positive-sequence current $\mathbf{I}^+_{\rm dqe} = [I_d I_q]^T$, and rotor speed $\omega_r$ as input information. By letting $R_f = 0$, $\hat{x_0}$ can be estimated. Using the estimated $\hat{x_0}$ value, the estimated power loss $\hat{P_f}$ can be calculated. $\hat{x_0}$ and $\hat{P_f}$ are utilized in the fault decision block, which should be configured based on the motor heat configuration and the drive environment.

Fig. 8(a) presents the proposed fault parameter estimation method. The proposed method utilizes a searching algorithm to find the minimum error between the applied negative-sequence voltage $|\mathbf{V}^-_{\rm dqe}|$ and the calculated $|\mathbf{V}^-_{\rm dqe}(\mathbf{k})|$ value while varying $x(k)$ from 1 (healthy) to 0 (fully faulty). $|\mathbf{V}^-_{\rm dqe}(\mathbf{k})|$ is obtained from the unbalanced voltage equations (4) and (5).

After fault parameter estimation, the Ohmic power loss can be calculated for ITF decisions and creation of a fault-tolerant drive. Based on $i_f$ and $i_{p1}$ from the model described in part I, the

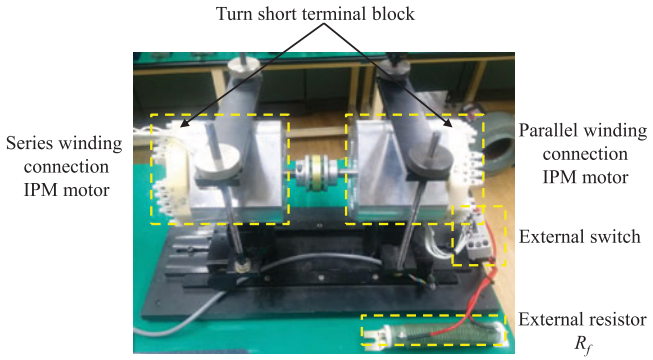


Fig. 10. Experimental setup.

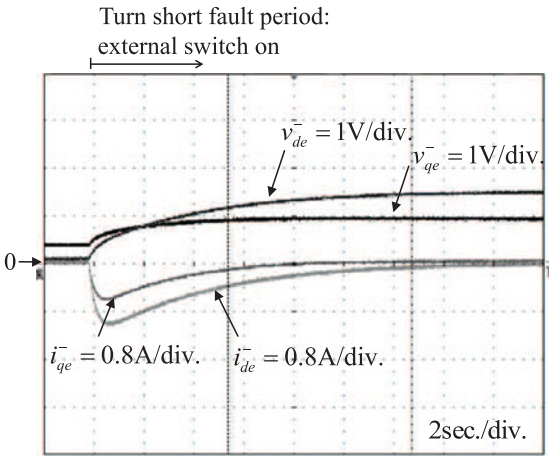


Fig. 11. Plots of negative-sequence voltages and currents in negative SRF when an ITF occurred.

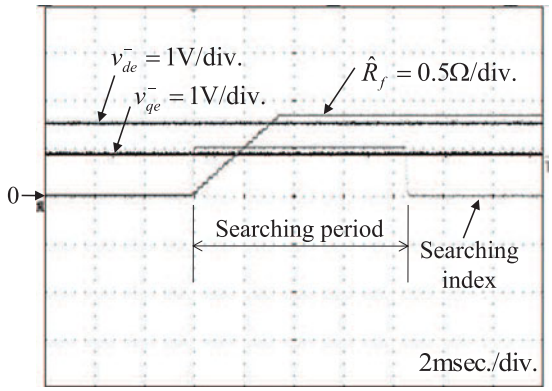


Fig. 12. Plots of $v_{\mathrm{de}}^{-}$, $v_{\mathrm{qe}}^{-}$, and estimated $R_f$ with proposed method at fixed $x$ for parallel winding IPMSM ($a$-phase winding fault, $R_f = 1\,\Omega$, 3500 r/min and $I_q = I_d = 0$).

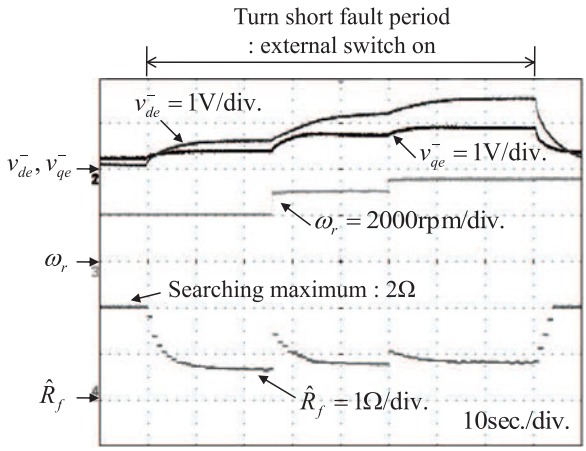


Fig. 13. Plots of $v_{\mathrm{de}}^{-}$, $v_{\mathrm{qe}}^{-}$, and continuously estimated $R_f$ values for parallel winding IPMSM ($a$-phase winding fault, $R_f = 1\,\Omega$, and $I_q = I_d = 0$).

Ohmic power loss $P_f$ of (15) and (16) can be derived as follows: (17) shown at the bottom of the page. For the estimated $\hat{x}_0$ value for $R_f = 0$, $P_f(R_f = 0, \hat{x}_0)$ can be simplified by eliminating the first term.

Additionally, the fault's phase can be determined based on the negative-sequence voltage phase

$$\theta_f = \tan^{-1}\left(\frac{V_{\mathrm{qe}}^{-}}{V_{\mathrm{de}}^{-}}.\right) \tag{18}$$

Here, (4) and (5) are obtained for the $a$-phase winding fault. For the $b$- and $c$-phase winding faults, the negative-sequence voltage has the same magnitude and $\pm 2\pi/3$ phase displacement relative to those in the $a$-phase fault. Fault phase winding detection might be meaningless if the motor drive stops and is changed immediately after the ITF is detected. However, the faulty phase winding can provide meaningful information for the creation of a fault-tolerant drive and troubleshooting. Fig. 9 plots the measured fault's phase angle $\theta_f$ and calculated fault's phase angles $\hat{\theta}_{\mathrm{fa}}$, $\hat{\theta}_{\mathrm{fb}}$, and $\hat{\theta}_{fc}$ in the negative SRF. $\hat{\theta}_{\mathrm{fa}}$, $\hat{\theta}_{\mathrm{fb}}$, and $\hat{\theta}_{fc}$ can be calculated when the magnitude of the negative-sequence voltage is the same as that of the measured $|\mathrm{V}_{\mathrm{dqe}}^{-}|$. After $\theta_f$ has been obtained, the faulty phase can be obtained by finding the minimum phase error for $\hat{\theta}_{\mathrm{fa}}$, $\hat{\theta}_{\mathrm{fb}}$, and $\hat{\theta}_{fc}$. In Fig. 9, $\theta_f$ is placed in the $a$-winding faulty phase range; thus, the ITF exists in one

$$P_f = \begin{cases} \left(\begin{array}{l} \frac{1}{2}R_f\sqrt{(I_d-\alpha_{s2})^2+(I_q+\alpha_{s1})^2} \\ +\frac{1}{2}R_{a1}(1-x)\left(\sqrt{\alpha_{s1}^2+\alpha_{s2}^2}-\sqrt{I_d^2+I_q^2}\right) \end{array}\right) & \text{: series winding IPMSM} \\ \left(\begin{array}{l} \frac{1}{2}R_f\sqrt{(\alpha_{p2}-\beta_{p2})^2+(\alpha_{p1}-\beta_{p1})^2}+\frac{1}{2}R_{a1}(1-x)\sqrt{\beta_{p2}^2+\beta_{p1}^2} \\ +\frac{1}{2}R_{a1}x\sqrt{\alpha_{p2}^2+\alpha_{p1}^2}+\frac{1}{P-2}R_{a1}\sqrt{(I_d-\alpha_{p2})^2+(I_q+\alpha_{p1})^2} \\ -\frac{1}{P}R_{a1}\sqrt{I_d^2+I_q^2} \end{array}\right) & \text{: parallel winding IPMSM} \end{cases} \tag{17}$$

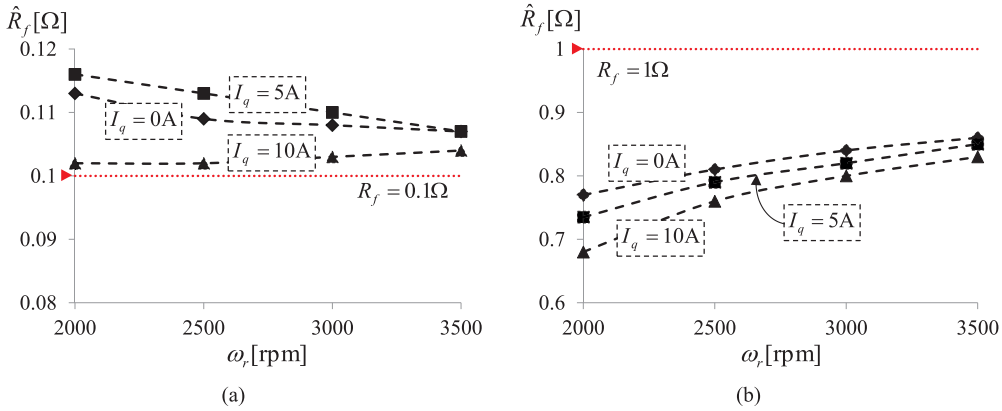


Fig. 14. Estimated values of $\hat{R}_f$ versus speed for various $q$-axis currents: (a) series and (b) parallel winding IPMSMs.

of the $a$-phase windings in this case. The searching process is shown in Fig. 8(b).

## IV. Experimental Results

Fig. 10 shows the experimental setup used for back-to-back IPMSM tests. One motor had series windings; the other had parallel windings. One IPMSM was operated as a motor, while the other was operated as a generator. The back of each IPMSM had an ITF terminal block that was connected to the intermediate stator windings. The external switch and resistor were series connected to the ITF terminal block of the test motor. When the external switch was turned OFF, the motors were healthy; when it was turned ON, an ITF occurred.

Fig. 11 plots the applied negative-sequence voltages ($v_{\rm de}^-$ and $v_{\rm qe}^-$) and currents ($i_{\rm de}^-$ and $i_{\rm qe}^-$) in the negative SRF when the ITF was generated by the external switch being turned ON at $t = 2$ s. Although there is no ITF for $t < 2$ s, the negative-sequence voltages have nonideal dc offsets. There are many reasons for dc offsets in the negative-sequence voltages, for example, motor eccentricity, an unbalanced drive output voltage due to nonidentical FETs or IGBTs, gain asymmetry of the phase current measurement, etc. After the external switch was turned ON, the negative-sequence currents $i_{\rm de}^-$ and $i_{\rm qe}^-$ occurred. Owing to the negative-sequence PI current controller, the generated $i_{\rm de}^-$ and $i_{\rm qe}^-$ values were regulated to be zero, which caused the negative-sequence voltages $v_{\rm de}^-$ and $v_{\rm qe}^-$ to increase to (and eventually sustain) nonzero values. The proposed method was utilized with $v_{\rm de}^-$ and $v_{\rm qe}^-$ to estimate the fault's phase and parameters.

Fig. 12 plots $v_{\rm de}^-$, $v_{\rm qe}^-$, and the estimated $\hat{R}_f$ value for $x = 0.5833$ (fixed) when the proposed estimation method was applied to the parallel winding IPMSM with an $a$-phase winding fault, $R_f = 1\,\Omega$, and $I_q = I_d = 0$. Under realistic conditions, the value of $x$ would be estimated under the assumption of $R_f = 0$, because $x$ is unknown. However, it was a known value in this controlled experiment, as we fixed $x$ at 0.5833. The estimated $\hat{R}_f$ value was compared to the external fault resistor's value $R_f$ to validate the estimation method. The proposed estimation method started searching $\hat{R}_f$ so as to satisfy the minimum negative-sequence voltage error at 6 ms and ended at 14 ms. The total calculation period was approximately 8 ms. The calculation period can be managed by changing $\delta_x$. Note that the model of the parallel IPMSM was more complex than that of the series IPMSM. Here, a DSP TMS320F28335 from Texas Instruments was utilized as the main microprocessor to control both the generator and the motor with a 5-kHz switching frequency. The proposed method was executed (with time to spare) after prioritizing the interrupt service routine of the control algorithm for the two IPMSMs. Because the ITF parameter did not change rapidly, the proposed estimation method did not need to be utilized frequently. Thus, the calculation time did not burden the microprocessor. Note that the experiments for the faulty phase winding search algorithm were omitted because it was easy to identify faults using only the ITF model.

Fig. 13 plots the continuous $\hat{R}_f$ estimation, while the motor speed was changed abruptly by the generator. The external switch was turned ON at approximately 1 s and OFFat 9 s. When the external switch was turned OFFfor $t < 1$ s and $t > 9$ s, $\hat{R}_f$ was $2\,\Omega$, which was the limiting value. Changing the motor speed caused $\hat{R}_f$ to pulse at the beginning, but it converged to a steady-state value immediately after $v_{\rm de}^-$ and $v_{\rm qe}^-$ converged.

It should be noted that every motor drive system has the dc offset voltage in the negative SRF, occurred by the unbalanced impedance, the structural problem, the sensor measurement error, etc., even under the healthy condition. It can be observed in Fig. 13 when the external switch is turned OFF($t < 1$ and $t > 9$). This dc offset voltage in the negative SRF reduces the estimation accuracy. The estimation results of this paper are obtained with the dc offset voltages. For better accurate estimation results, the dc offset voltage can be compensated with a lookup table method which should be built in advance. Fig. 14 plots the estimation results of $\hat{R}_f$ for (a) series ($R_f = 0.1$) and (b) parallel ($R_f = 0.1$) winding IPMSMs after compensating the dc offset voltage. It can be observed that the accuracy increased with the speed because of the larger negative-sequence voltage from the ITF. Note also that the estimation was more accurate for the series winding IPMSM.

## V. Concluding Remarks

This paper proposed a fault parameter estimation method for ITFs in IPMSMs employing series and parallel winding connections. We proved that the negative-sequence voltage and additional power loss due to the ITF are functions of $f_{\rm xR}(x, R_f)$.

For a given ITF condition, $f_{\mathrm{xR}}$ has a constant value; therefore, there are multiple pairs of solutions for $x$ and $R_f$ that satisfy $f_{\mathrm{xR}} = \mathrm{constant}$. If we arbitrarily set the value for either $x$ or $R_f$, the other value is determined by $f_{\mathrm{xR}} = \mathrm{constant}$. However, the additional power loss, which is the most important cause of deterioration due to faults, is still a function of the constant $f_{\mathrm{xR}}$ and independent of both fault parameter values. Thus, using $R_f = 0$ in the simple calculation, an $\hat{x_0}$ estimation method based on the searching algorithm can be proposed. The proposed estimation method was validated experimentally.

## REFERENCES


[1] I. Jeong, B. J. Hyon, and K. Nam, "Dynamic modeling and control for SPMSMs with internal turn short faults," *IEEE Trans. Power Electron.*, vol. 28, no. 7, pp. 3495–3508, Jul. 2013.

[2] B. G. Gu, J. H. Choi, and I. S. Jung, "Development and analysis of inter-turn short fault model of PMSMs with series and parallel winding connections," *IEEE Trans. Power Electron.*, vol. 29, no. 4, pp. 2016–2026, Apr. 2014.

[3] M. A. Cash, T. G. Habetler, and G. B. Kliman, "Insulation failure prediction in AC machines using line-neutral voltages," *IEEE Trans, Ind. Appl.*, vol. 34, no. 6, pp. 1234–1239, Nov./Dec. 1998.

[4] A. J. M. Cardoso, S. M. A. Cruz, and D. S. B. Fonseca, "Inter-turn stator winding fault diagnosis in three-phase induction motors, by Park's vector approach," *IEEE Trans. Energy Convers.*, vol. 14, no. 3, pp. 595–598, Sep. 1999.

[5] M. Arkan, D. L. Perovic, and P. Unswoth, "On-line stator winding fault diagnosis in induction motors," *IEE Proc. Elect. Power Appl.*, vol. 148, no. 6, pp. 537–547, Nov. 2001.

[6] F. Briz, M. W. Degner, A. Zamarron, and J. M. Guerrero, "Online stator winding fault diagnosis in inverter-fed AC machines using high-frequency signal injection," *IEEE Trans. Ind. Appl.*, vol. 39, no. 4, pp. 1109–1117, Jul./Aug. 2003.

[7] R. M. Tallam, T. G. Habetler, and R. G. Harley, "Stator winding turn-fault detection for closed-loop induction motor drives," *IEEE Trans. Ind. Appl.*, vol. 39, no. 3, pp. 720–724, May/Jun. 2003.

[8] S. B. Lee, R. M. Tallam, and T. G. Habetler, "A robust, on-line turn-fault detection technique for induction machines base on monitoring the sequence component impedance matrix," *IEEE Trans. Power Electron.*, vol. 18, no. 3, pp. 865–872, May 2003.

[9] R. M. Tallam, S. B. Lee, G. C. Stone, G. B. Kliman, J. Yoo, T. G. Habetler, and R. G. Harley, "A survey of methods for detection of stator-related faults in induction machines," *IEEE Trans. Ind. Appl.*, vol. 43, no. 4, pp. 920–933, Jul. 2007.

[10] J. Yun, K. Lee, K. W. Lee, S. B. Lee, and J. Y. Yoo, "Detection and classification of stator turn faults and high-resistance electrical connections for induction machines," *IEEE Trans. Ind. Appl.*, vol. 45, no. 2, pp. 666–675, Mar./Apr. 2009.

[11] S. Cheng, P. Zhang, and T. G. Habetler, "An impedance identification approach to sensitive detection and location of stator turn-to-turn faults in a closed-loop multiple-motor drive," *IEEE Trans. Ind. Electron.*, vol. 58, no. 5, pp. 1545–1554, May 2011.

[12] P. Ostojic, A. Banerjee, D. C. Patel, W. Basu, and S. Ali, "Advanced motor monitoring and diagnostics," *IEEE Trans. Ind. Appl.*, vol. 50, no. 5, pp. 3120–3127, Sep./Oct. 2014.

[13] M. Eftekhari, M. Moallem, S. Sadri, and M. F. Hsieh, "Online detection of induction motors stator winding short-circuit faults," *IEEE Syst. J.*, vol. 8, no. 4, pp. 1272–1282, Dec. 2014.

[14] M. A. Awadallah, M. M. Morcos, S. Gopalakrishnan, and T. W. Nehl, "A neuro-fuzzy approach to automatic diagnosis and location of stator inter-turn fault in CSI-Fed PM brushless DC motors," *IEEE Trans. Energy Conv.*, vol. 20, no. 2, pp. 253–259, Jun. 2005.

[15] K. T. Kim, S. T. Lee, and J. Hur, "Diagnosis technique using a detection coil in BLDC motors with interturn faults," *IEEE Trans. Magn.*, vol. 50, no. 2, art. no. 7022004, Feb. 2014.

[16] J. K. Park, C. L. Jeong, S. T. Lee, and J. Hur, "Early detection technique for stator winding inter-turn fault in BLDC motor using input impedance," *IEEE Trans. Ind. Appl.*, vol. 51, no. 1, pp. 240–247, Jan./Feb. 2015.

[17] S. Cheng and T. G. Habetler, "Using only the DC current information to detect stator turn faults in automotive claw-pole generators," *IEEE Trans. Ind. Electron.*, vol. 60, no. 8, pp. 3462–3471, Aug. 2013.

[18] P. Neti and S. Nandi, "Stator interturn fault detection of synchronous machines using field current and rotor search-coil voltage signature analysis," *IEEE Trans. Ind. Appl.*, vol. 45, no. 3, pp. 911–920, May/Jun. 2009.

[19] K. H. Kim, B. G. Gu, and I. S. Jung, "Online fault-detecting scheme of an inverter-fed permanent magnet synchronous motor under stator winding shorted turn and inverter switch open," *IET Electric Power Appl.*, vol. 5, no. 6, pp. 529–539. 2010.

[20] B. M. Ebrahimi and J. Faiz, "Feature extraction for short-circuit fault detection in permanent-magnet synchronous motors using stator-current monitoring," *IEEE Trans. Power Electron.*, vol. 25, no. 10, pp. 2673–2682, Oct. 2010.

[21] M. Hadef, A. Djerdir, M. R. Mekideche, and A-O. N'Diaye, "Diagnosis of stator winding short circuit faults in a direct torque controlled interior permanent magnet synchronous motor," in *Proc. IEEE Veh. Power Propul. Conf.*, 2011, pp. 1–8.

[22] A. Gandhi, T. Corrigan, and L. Parsa, "Recent advances in modeling and online detection of stator interturn faults in electrical motors," *IEEE Trans. Ind. Electron.*, vol. 58, no. 5, pp. 1564–1575, May 2011.

[23] A. Sarikhani and O. A. Mohammed, "Inter-turn fault detection in PM synchronous machines by physics-based back electromotive force estimation," *IEEE Trans. Ind. Electron.*, vol. 60, no. 8, pp. 3472–3484, Aug. 2013.


B.-G. Gu, photograph and biography not available at the time of publication.